

Single-Scattering Optical Tomography

Vadim A. Markel and John C. Schotland

Departments of Radiology and Bioengineering, University of Pennsylvania,
Philadelphia, PA 19104

Abstract. We describe a novel tomographic imaging modality. The proposed technique utilizes visible or near-infrared light as a tissue probe in the “mesoscopic” scattering regime when the tissue layer exhibits sufficiently strong scattering so that its direct visual inspection is not possible, yet transmitted and reflected light are not diffuse. The forward model for light propagation in tissues is based on the scattering-order expansion of the radiative transport equation Green’s function. The associated inverse problem is similar to the problem of inverting the Radon transform of x-ray tomography, except that the ray integrals are evaluated not along straight lines but along broken rays. As a result, the method does not require rotating the imaging device around the sample and taking multiple projections and, therefore, can be used in backscattering. An algebraic image reconstruction algorithm is numerically implemented using computer-generated data. An analytic image reconstruction formula analogous to the filtered backprojection formula of x-ray tomography is derived.

1. Introduction

We describe here a novel optical imaging modality which utilizes near-infrared or visible light to probe the structure of tissue. The proposed technique will work in the “intermediate” scattering regime. Namely, we are interested in the physical situation when tissue exhibits sufficient scattering that the image reconstruction methods of computed tomography (based on inverting the Radon transform) are not applicable, yet the detected light is not diffuse and can be described by a low order scattering approximation to the radiative transport equation (RTE). The principle idea is to measure single-scattered light by means of angularly-selective detectors and to use these measurements to reconstruct the tissue optical properties by solving an appropriate inverse scattering problem. We will refer to this technique as the **single scattering optical tomography** (SSOT).

2. The Principle of SSOT

The physical principle of SSOT is quite simple and is illustrated in Fig. 1. Here the sample has the shape of a slab and, for the sake of simplicity, incident beams enter through one of its surfaces normally. However, more general incidence angles are considered below in section 3.

In the absence of scattering, the incident beam would propagate straight through the slab, as shown by the green ray. Detection of such straight (unscattered) rays is the basis of computerized x-ray tomography. If there is finite scattering in the medium, the ray can “change direction” as shown in Fig. 1(a). Of course, scattering does not result in elimination of the ballistic ray. However, it is possible to employ angle-selective detectors that do not register the ballistic component of transmitted light. In the example shown in Fig. 1(a), only the intensity of the broken ray shown by the red line is detected. We will refer to the latter as the *single-scattered ray* (SSR). Further, it is not difficult to see that the two points on the slab surface (the point where the incident beam enters the medium and the point at which the detected ray exists the medium) and the incidence and detection angles uniquely define a ray trajectory, assuming that only one scattering event has occurred (the ray in question has only one node). It will be shown below that the intensity measured by the detector is mathematically related to the integral of the attenuation coefficient for the probing light taken along the SSR. In this respect, the mathematical structure of SSOT is similar to that of Radon transform, except that the integrals are evaluated along broken rays.

By utilizing multiple incident beams and detecting light exiting the medium at different points, as shown in Fig. 1(b), it is possible to collect enough data to reconstruct the spatial distribution of the attenuation coefficient in the selected slice of the slab. Three-dimensional reconstruction can then be performed slice-by-slice. In addition to varying the incident and exit points, one can also vary the incident and exit angles. This can provide additional information for simultaneous reconstruction of absorption

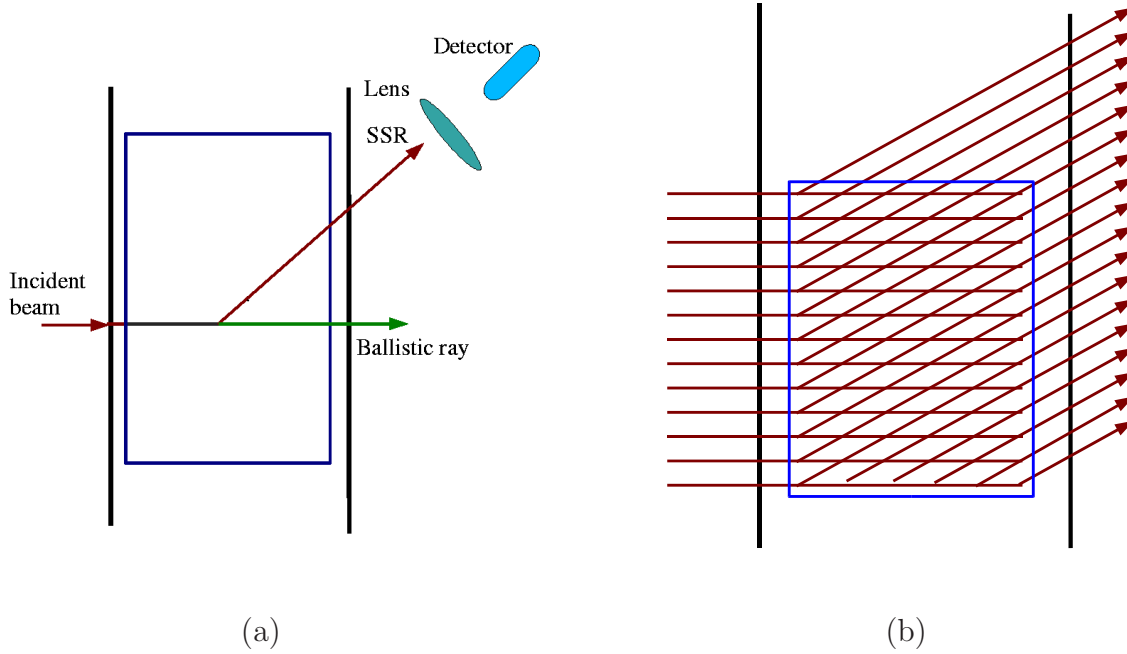


Figure 1. (a) Schematic illustration of the SSR trajectory. (b) Source-detector arrangement for SSOT. Reconstruction is performed independently slice-by slice. The blue rectangle represents the area in which reconstruction can be performed.

and scattering coefficients of the sample.

As can be seen, the single-scattered component is selected by making the source and detector both angularly-selective but not aligned with each other. The fact that the source and detector are not on axis allows one to neglect the ballistic component of transmitted light. The data can be collected either on opposite sides of the slab (transmission measurements), or in the backscattering geometry. In both cases, rotation of the device around the sample is not required.

3. Mathematical Formulation of SSOT

In radiative transport theory, light propagating through the medium is described by specific intensity $I(\mathbf{r}, \hat{\mathbf{s}})$ at the point \mathbf{r} flowing in the direction $\hat{\mathbf{s}}$. The specific intensity is directly measurable with appropriate detectors ‡. The time-independent RTE reads

$$[\hat{\mathbf{s}} \cdot \nabla + \mu_a(\mathbf{r}) + \mu_s(\mathbf{r})] I(\mathbf{r}, \hat{\mathbf{s}}) = \mu_s(\mathbf{r}) \int A(\hat{\mathbf{s}}, \hat{\mathbf{s}}') I(\mathbf{r}, \hat{\mathbf{s}}') d^2 \hat{\mathbf{s}}' , \quad \mathbf{r} \in V , \quad (1)$$

where V is a spatial region, $\mu_a(\mathbf{r})$ and $\mu_s(\mathbf{r})$ are the absorption and scattering coefficients (generally, position-dependent) and $A(\hat{\mathbf{s}}, \hat{\mathbf{s}}')$ is the scattering kernel normalized according to the condition $\int A(\hat{\mathbf{s}}, \hat{\mathbf{s}}') d^2 \hat{\mathbf{s}}' = 1$. Eq. (1) is supplemented by inhomogeneous boundary

‡ More precisely, the detectors usually measure an integral of the specific intensity over some small solid angle and a finite aperture.

condition of the form

$$I(\mathbf{r}, \hat{\mathbf{s}})|_{\mathbf{r} \in \Omega} = I_{\text{inc}}(\mathbf{r}, \hat{\mathbf{s}})|_{\mathbf{r} \in \Omega} , \quad \text{if } \hat{\mathbf{s}} \cdot \hat{\mathbf{n}}(\mathbf{r}) < 0 , \quad (2)$$

where $\Omega = \partial V$ is the boundary of V , $\hat{\mathbf{n}}(\mathbf{r})$ is the outward unit normal to this surface at the point $\mathbf{r} \in \Omega$ and $I_{\text{inc}}(\mathbf{r}, \hat{\mathbf{s}})|_{\mathbf{r} \in \Omega}$ is the incident specific intensity at the boundary. The integro-differential equation (1) with the boundary conditions (2) can be equivalently re-written as an integral equation:

$$I(\mathbf{r}, \hat{\mathbf{s}}) = I_b(\mathbf{r}, \hat{\mathbf{s}}) + \int G_b(\mathbf{r}, \hat{\mathbf{s}}; \mathbf{r}', \hat{\mathbf{s}}') \mu_s(\mathbf{r}') A(\hat{\mathbf{s}}', \hat{\mathbf{s}}'') I(\mathbf{r}', \hat{\mathbf{s}}'') d^3 r' d^2 \hat{\mathbf{s}}' d^2 \hat{\mathbf{s}}'' . \quad (3)$$

Here $I_b(\mathbf{r}, \hat{\mathbf{s}})$ is the ballistic component of specific intensity and $G_b(\mathbf{r}, \hat{\mathbf{s}}; \mathbf{r}', \hat{\mathbf{s}}')$ is the ballistic Green's function of the RTE. The ballistic intensity satisfies

$$[\hat{\mathbf{s}} \cdot \nabla + \mu_a(\mathbf{r}) + \mu_s(\mathbf{r})] I_b(\mathbf{r}, \hat{\mathbf{s}}) = 0 \quad (4)$$

with the inhomogeneous boundary condition (2). If an incident narrow collimated beam of total power I_0 enters the medium at the point \mathbf{r}_1 in the direction $\hat{\mathbf{s}}_1$, then $I_b(\mathbf{r}, \hat{\mathbf{s}})$ is given by the following formula:

$$I_b(\mathbf{r}, \hat{\mathbf{s}}) = I_0 G_b(\mathbf{r}, \hat{\mathbf{s}}; \mathbf{r}_1, \hat{\mathbf{s}}_1) , \quad (5)$$

where the ballistic Green's function $G_b(\mathbf{r}, \hat{\mathbf{s}}; \mathbf{r}', \hat{\mathbf{s}}')$ is given by

$$G_b(\mathbf{r}, \hat{\mathbf{s}}; \mathbf{r}', \hat{\mathbf{s}}') = g_b(\mathbf{r}, \mathbf{r}') \delta_2[\hat{\mathbf{u}}(\mathbf{r} - \mathbf{r}') - \hat{\mathbf{s}}'] \delta_2(\hat{\mathbf{s}} - \hat{\mathbf{s}}') , \quad (6)$$

$$g_b(\mathbf{r}, \mathbf{r}') = \frac{1}{|\mathbf{r} - \mathbf{r}'|^2} \exp \left[- \int_0^{|\mathbf{r} - \mathbf{r}'|} \mu_t(\mathbf{r}' + \ell \hat{\mathbf{u}}(\mathbf{r} - \mathbf{r}')) d\ell \right] . \quad (7)$$

Here $\delta_2(\hat{\mathbf{s}} - \hat{\mathbf{s}}')$ is the two-dimensional delta-function of direction which is zero unless $\hat{\mathbf{s}}$ coincides with $\hat{\mathbf{s}}'$, $\hat{\mathbf{u}}(\mathbf{r}) = \mathbf{r}/r$ is a unit vector in the direction of an arbitrary vector \mathbf{r} , and we have introduced the total extinction (attenuation) coefficient $\mu_t(\mathbf{r}) = \mu_a(\mathbf{r}) + \mu_s(\mathbf{r})$. Note that g_b is the angularly-averaged ballistic Green's function:

$$g_b(\mathbf{r}, \mathbf{r}') = \int d^2 \hat{\mathbf{s}} d^2 \hat{\mathbf{s}}' G_b(\mathbf{r}, \hat{\mathbf{s}}; \mathbf{r}', \hat{\mathbf{s}}') . \quad (8)$$

The scattering-order expansion is obtained by iterating Eq. (3) starting from $I = I_b$. Generally, this results in $I = I_b + I_s$, where the scattered component I_s is expressible as a series. If the expansion is terminated at the first order, we obtain the following expression for I_s :

$$I_s(\mathbf{r}, \hat{\mathbf{s}}) = \int G_b(\mathbf{r}, \hat{\mathbf{s}}; \mathbf{r}', \hat{\mathbf{s}}') \mu_s(\mathbf{r}') A(\hat{\mathbf{s}}', \hat{\mathbf{s}}'') I_b(\mathbf{r}', \hat{\mathbf{s}}'') d^3 r' d^2 \hat{\mathbf{s}}' d^2 \hat{\mathbf{s}}'' . \quad (9)$$

Let the incident beam of intensity I_0 enter the slab of width L at the point \mathbf{r}_1 and in the direction $\hat{\mathbf{s}}_1$ while the detector registers the ray exiting the slab through the opposite surface at the point \mathbf{r}_2 and in the direction $\hat{\mathbf{s}}_2$. We denote the intensity measured in

such experiment by $I_s(\mathbf{r}_2, \hat{\mathbf{s}}_2; \mathbf{r}_1, \hat{\mathbf{s}}_1)$. Then integration according to (9) with $I_b(\mathbf{r}', \hat{\mathbf{s}}')$ given by (5) yields

$$I_s(\mathbf{r}_2, \hat{\mathbf{s}}_2; \mathbf{r}_1, \hat{\mathbf{s}}_1) = I_0 \Theta(\pi - \theta_1 - \theta_2) \delta(|\varphi_{\hat{\mathbf{s}}_1} - \varphi_{\hat{\mathbf{s}}_2}| - \pi) \frac{\mu_s(\mathbf{R}_{21}) A(\hat{\mathbf{s}}_2, \hat{\mathbf{s}}_1)}{r_{21} \sin \theta_1 \sin \theta_2} \\ \times \exp \left[- \int_0^{L_1} \mu_t(\mathbf{r}_1 + \ell \hat{\mathbf{s}}_1) d\ell - \int_0^{L_2} \mu_t(\mathbf{R}_{21} + \ell \hat{\mathbf{s}}_2) d\ell \right], \quad (10)$$

where the term $\delta(|\varphi_{\hat{\mathbf{s}}_1} - \varphi_{\hat{\mathbf{s}}_2}| - \pi)$ is explained below, $\Theta(x)$ is the step function, \mathbf{R}_{21} is the position of the node (the ray turning point), $\mathbf{r}_{21} = \mathbf{r}_2 - \mathbf{r}_1$, $r_{21} = |\mathbf{r}_{21}|$, $L_1 = |\mathbf{R}_{21} - \mathbf{r}_1|$, $L_2 = |\mathbf{r}_2 - \mathbf{R}_{21}|$, and the angles θ_1 and θ_2 are defined by $\cos \theta_{1,2} = \hat{\mathbf{r}}_{21} \cdot \hat{\mathbf{s}}_{1,2}$ (see Fig. 2 for an illustration). We note the following relations:

$$\mathbf{R}_{21} = \mathbf{r}_1 + L_1 \hat{\mathbf{s}}_1 = \mathbf{r}_2 - L_2 \hat{\mathbf{s}}_2 \quad (11)$$

$$L_1 = r_{21} \frac{\sin \theta_2}{\sin(\theta_1 + \theta_2)}, \quad L_2 = r_{21} \frac{\sin \theta_1}{\sin(\theta_1 + \theta_2)}, \quad (12)$$

We now discuss the physical meaning of various terms in (10). First, the angles $\varphi_{\hat{\mathbf{s}}_{1,2}}$ in the expression $\delta(|\varphi_{\hat{\mathbf{s}}_1} - \varphi_{\hat{\mathbf{s}}_2}| - \pi)$ are the azimuthal angles of unit vectors $\hat{\mathbf{s}}_{1,2}$ in a reference frame whose z -axis intersects both the position of the source and the detector (this axis is shown by a dashed line in Fig. 2 and should not be confused with the z -axis of the laboratory frame shown by a solid line in the same figure). The presence of the above one-dimensional delta function in Eq. (10) is the mathematical manifestation of the fact that two straight rays exiting from the points \mathbf{r}_1 and \mathbf{r}_2 in the directions $\hat{\mathbf{s}}_1$ and $-\hat{\mathbf{s}}_2$, respectively, can intersect only if $\hat{\mathbf{s}}_1$ and $\hat{\mathbf{s}}_2$ and \mathbf{r}_{21} are in the same plane (equivalently, if $\varphi_{\hat{\mathbf{s}}_1} - \varphi_{\hat{\mathbf{s}}_2} = 0, \pm\pi$) and point into different half-planes (this requires that $\varphi_{\hat{\mathbf{s}}_1} - \varphi_{\hat{\mathbf{s}}_2} = \pm\pi$). Second, the point of intersection exists only if $\theta_1 + \theta_2 < \pi$, which is expressed by the theta-function $\Theta(\pi - \theta_1 - \theta_2)$. We note that if, additionally, $\hat{\mathbf{s}}_1$ and $\hat{\mathbf{s}}_2$ are restricted such that $\hat{\mathbf{z}} \cdot \hat{\mathbf{s}}_1 > 0$ and $\hat{\mathbf{z}} \cdot \hat{\mathbf{s}}_2 < 0$ ($\hat{\mathbf{s}}_1$ points into the slab and $\hat{\mathbf{s}}_2$ points out of the slab), then \mathbf{R}_{21} is within the slab. Third, the factor $\mu_s(\mathbf{R}_{21}) A(\hat{\mathbf{s}}_2, \hat{\mathbf{s}}_1)$ is the ‘‘probability’’ that the ray is scattered at the point $\mathbf{r} = \mathbf{R}_{21}$ and changes direction from $\hat{\mathbf{s}}_1$ to $\hat{\mathbf{s}}_2$. This factor is, in general, position-dependent. Fourth, $1/r_{21} \sin \theta_1 \sin \theta_2$ is a geometrical factor. We note that it can be equivalently rewritten as $r_{21}/H_{21}H_{12}$, where H_{21} and H_{12} are the two heights of the triangle $(\mathbf{r}_1, \mathbf{R}_{21}, \mathbf{r}_2)$ drawn from the vertices \mathbf{r}_1 and \mathbf{r}_2 , respectively, as shown in Fig. 2. Derivation of this geometrical factor is somewhat involved; more detail is given in Appendix A. Finally, the integral of the attenuation function in the argument of the exponent is evaluated along the SSR.

Eq. (10) is the mathematical departure point for image reconstruction. In general, both the scattering and absorption coefficient can be reconstructed independently. We, however, consider first the more simple case when μ_s and the phase function $A(\hat{\mathbf{s}}, \hat{\mathbf{s}}')$ are constant and known. We then define the data function as

$$\phi(\mathbf{r}_2, \hat{\mathbf{s}}_2; \mathbf{r}_1, \hat{\mathbf{s}}_1) = - \ln \left[\frac{r_{21} \sin \theta_1 \sin \theta_2 \int I_s(\mathbf{r}_2, \hat{\mathbf{s}}_2; \mathbf{r}_1, \hat{\mathbf{s}}_1) d\varphi_{\hat{\mathbf{s}}_2}}{I_0 \mu_s A(\hat{\mathbf{s}}_2, \hat{\mathbf{s}}_1)} \right]. \quad (13)$$

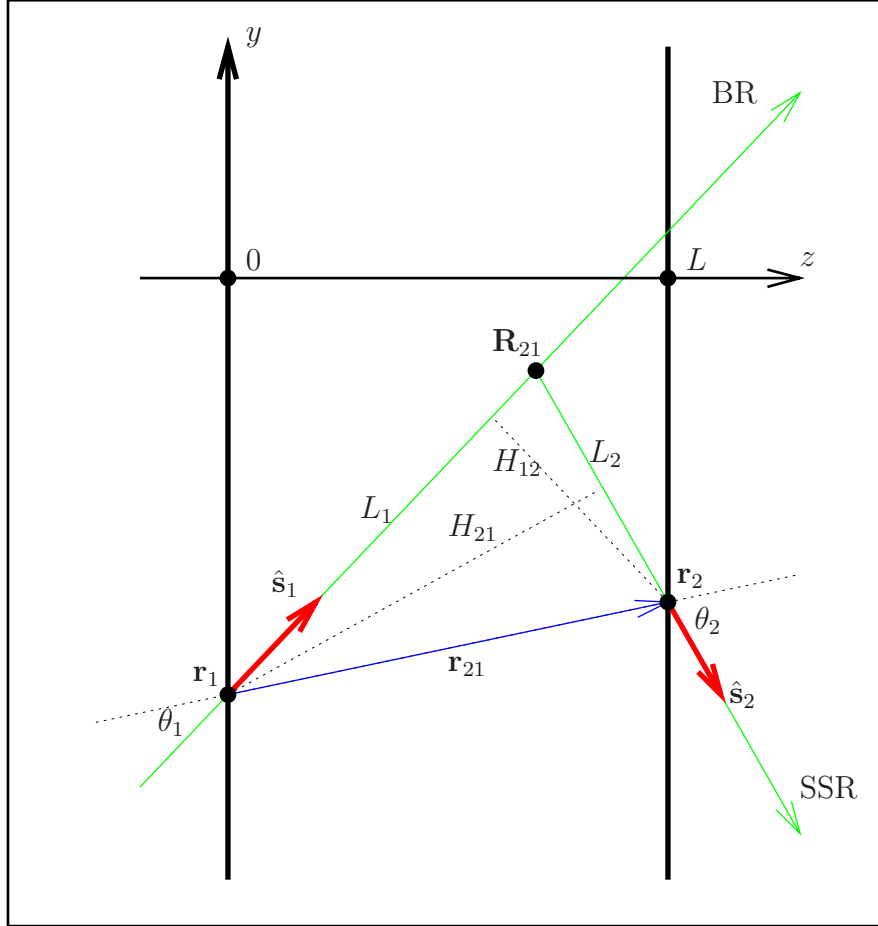


Figure 2. Geometrical illustration of the quantities used in Eq. (10) and elsewhere. “BR” denotes ballistic ray and “SSR” denotes single-scattered ray.

Note that if I_s is experimentally measured, the angular integration in the right-hand side of (13) does not need to be performed numerically. The measured data is already integrated in a narrow interval of $\varphi_{\hat{s}_2}$ due to the finite aperture and acceptance angle of the detector. Note also that the above definition is only applicable for such configuration of sources and detectors that $\theta_1 + \theta_2 < \pi$. Otherwise, any measured intensity is due to higher-order terms in the scattering-order expansion which are not properly described by formula (10).

By combining definition (13) and Eq. (10), we find that the attenuation function satisfies the following linear equation:

$$\int_{\text{SSR}(\mathbf{r}_2, \hat{\mathbf{s}}_2; \mathbf{r}_1, \hat{\mathbf{s}}_1)} \mu_t[\mathbf{r}(\ell)] d\ell = \phi(\mathbf{r}_2, \hat{\mathbf{s}}_2; \mathbf{r}_1, \hat{\mathbf{s}}_1) . \quad (14)$$

Here the integral $\int_{\text{SSR}} d\ell$ is evaluated along the SSR which is uniquely defined by the source and detector positions and orientations and ℓ is the linear coordinate on this ray. Thus, the inverse problem of SSOT is, essentially, linear, even though we did not

make any assumptions about the function $\mu_t(\mathbf{r})$. In this respect, SSOT is similar to the problem of inverting the Radon transform in x-ray tomography.

We next notice that the inverse problem of finding $\mu_t(\mathbf{r})$ in a selected slice given the complete set of measurements $\phi(\mathbf{r}_1, \hat{\mathbf{s}}_1; \mathbf{r}_2, \hat{\mathbf{s}}_2)$ is overdetermined. That is, the unknown function is two-dimensional while the data are four-dimensional since it depends, in general, on two spatial and two angular variables. This creates an opportunity for simultaneous reconstruction of scattering and absorption coefficients. Indeed, let $\mu_s(\mathbf{r})$ be variable and let the background (or average) value of the scattering coefficient be $\langle \mu_s \rangle$. Then Eq. (14) is generalized to

$$\int_{\text{SSR}(\mathbf{r}_2, \hat{\mathbf{s}}_2; \mathbf{r}_1, \hat{\mathbf{s}}_1)} \mu_t[\mathbf{r}(\ell)] d\ell - \ln \left[\frac{\mu_s(\mathbf{R}_{21})}{\langle \mu_s \rangle} \right] = \phi(\mathbf{r}_2, \hat{\mathbf{s}}_2; \mathbf{r}_1, \hat{\mathbf{s}}_1) , \quad (15)$$

where the background value $\langle \mu_s \rangle$ must be used in the definition (13) of ϕ . Eq. (15) can be solved with respect to the two sets of unknowns, $\mu_t(\mathbf{r})$ and $\ln[\mu_s(\mathbf{r})/\langle \mu_s \rangle]$. From these two solutions, $\mu_a(\mathbf{r})$ and $\mu_s(\mathbf{r})$ can be separately defined.

4. Image Reconstruction Formula

Eq. (14) can be discretized and solved by standard methods of linear algebra. This approach is taken in the numerical part of this paper (section 5 below). However, more sophisticated image reconstruction methods which utilize the translational invariance of rays are also possible. These methods are conceptually similar to those we have previously developed for optical diffuse optical tomography [1–5]. In particular, we describe here how an explicit image reconstruction formula can be obtained for fixed incidence and detection angles, e.g., in the situation schematically shown in Fig. 1(b).

As was explained above, selection of the point of incidence \mathbf{r}_1 , point of detection \mathbf{r}_2 and the direction of incidence $\hat{\mathbf{s}}_1$ defines a slice in which image reconstruction of SSOT is performed. In Fig. 2, this slice coincides with the YZ -plane of the laboratory frame. Assuming that the x -coordinate is fixed, we view the attenuation coefficient as a two-dimensional function $\mu_t = \mu_t(y, z)$ and focus on two-dimensional image reconstruction in the selected slice.

Since the unknown function is two-dimensional, it is sufficient to consider only two-dimensional measurements. One possible choice is to scan the incidence and detection points y_1 and y_2 while keeping the incidence and detection angles β_1 and β_2 fixed. By incidence and detection angles we mean here the angles between the z -axis of the laboratory frame and the unit vectors $\hat{\mathbf{s}}_1$ and $\hat{\mathbf{s}}_2$, respectively, as shown in Fig. 3. These angles are not equal to θ_1 and θ_2 shown in Fig. 2. The latter can vary in the measurement scheme described in this section, while β_1 and β_2 are fixed. Below, we omit β_1 and β_2 from the list of formal arguments of the data function and consider the following equation

$$\int_{\text{SSR}(y_2, y_1)} \mu_t[y(\ell), z(\ell)] d\ell = \phi(y_2, y_1) , \quad (16)$$

where $\phi(y_2, y_1)$ is the two-dimensional data function.

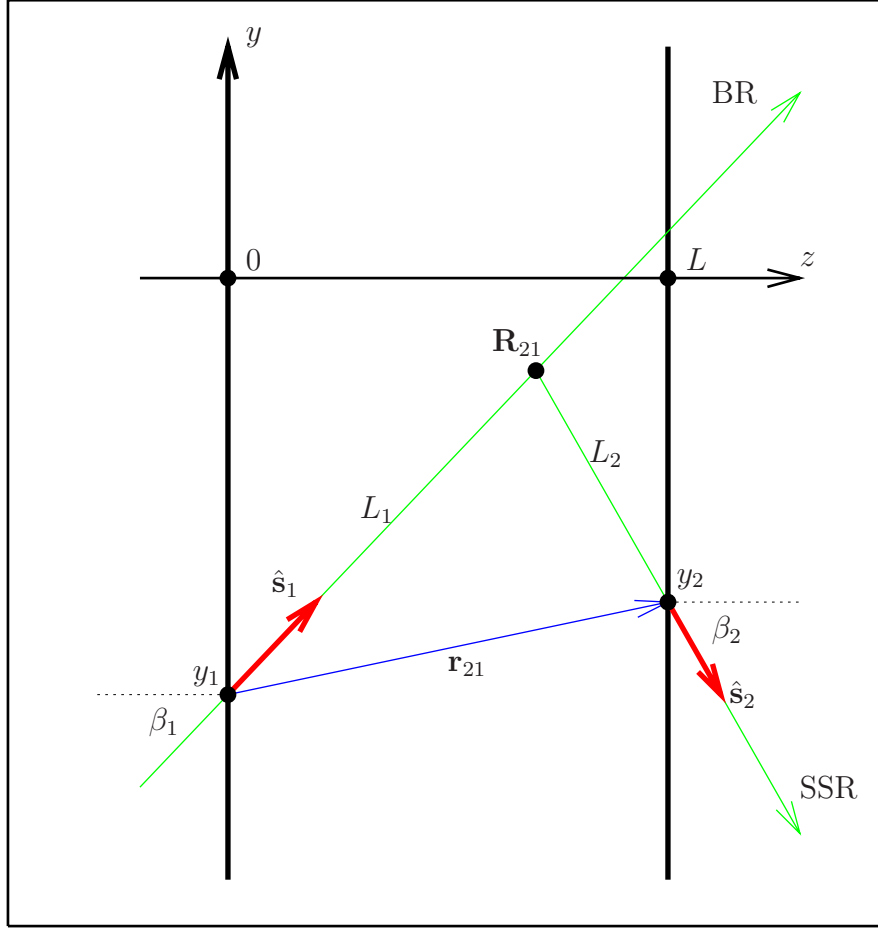


Figure 3. Definition of incidence and detection angles β_1 and β_2 for the measurement scheme described in section 4.

Next, we introduce a change of variables. Let $\psi(y_1, \Delta y) = \phi(y_1 + \Delta y, y_1)$. We thus view the data as a function of the source position y_1 and the source-detector transverse separation Δy . The important point is that the shape of the SSR depends only on Δy but not on y_1 . We, therefore, can write in the integrand of Eq. (16)

$$y(\ell) = y_1 + \eta(\Delta y, \ell) , \quad (17)$$

$$z(\ell) = \zeta(\Delta y, \ell) . \quad (18)$$

Here the functions η and ζ depend on Δy and ℓ (and, implicitly, on β_1 and β_2), but not on y_1 . This prompts that Eq. (16) can be simplified by Fourier transforming it with respect to y_1 . Indeed, this results in the following one-dimensional equation:

$$\int_0^{L_1+L_2} \exp[-ik\eta(\Delta y, \ell)] \tilde{\mu}_t[k, \zeta(\Delta y, \ell)] d\ell = \tilde{\psi}(k, \Delta y) , \quad (19)$$

where we have defined Fourier transforms of $\psi(y_1, \Delta y)$ and $\mu_t(y, z)$ according to

$$\tilde{\psi}(k, \Delta y) = \int_{-\infty}^{\infty} \psi(y_1, \Delta y) \exp(iky_1) dy_1 , \quad (20)$$

$$\psi(y_1, \Delta y) = \int_{-\infty}^{\infty} \tilde{\psi}(k, \Delta y) \exp(-iky_1) \frac{dk}{2\pi} , \quad (21)$$

$$\tilde{\mu}_t(k, z) = \int_{-\infty}^{\infty} \mu_t(y, z) \exp(iky) dy , \quad (22)$$

$$\mu(y, z) = \int_{-\infty}^{\infty} \tilde{\mu}_t(k, z) \exp(-iky) \frac{dk}{2\pi} . \quad (23)$$

Thus, the two-dimensional integral equation (16) has been reduced to the one-dimensional integral equation (19) which is parameterized by the Fourier variable k .

Integral equation (19) can be inverted analytically. For simplicity, we have derived an analytical solution in the special case of normal incidence, $\beta_1 = 0$, while the detection angle β_2 is arbitrary. We then have

$$\eta(\Delta y, \ell) = \begin{cases} 0 , & \ell < L_1(\Delta y) \\ [\ell - L_1(\Delta y)] \sin \beta_2 , & L_1(\Delta y) < \ell < L_1(\Delta y) + L_2(\Delta y) \end{cases} , \quad (24)$$

$$\zeta(\Delta y, \ell) = \begin{cases} \ell , & \ell < L_1(\Delta y) \\ L_1(\Delta y) + [\ell - L_1(\Delta y)] \cos \beta_2 , & L_1(\Delta y) < \ell < L_1(\Delta y) + L_2(\Delta y) \end{cases} . \quad (25)$$

Here $L_1(\Delta y) = L - \Delta y \operatorname{ctg} \beta_2$, $L_2(\Delta y) = \Delta y / \sin \beta_2$ and the allowable values of Δy are in the range $[0, L \operatorname{tg} \beta_2]$; the total length of the ray is $L_1 + L_2 = L + \Delta y \operatorname{tg}(\beta_2/2)$. In particular, note that $L_1 \leq L$, where L is the total slab thickness. We now substitute expressions (24),(25) into (19) and, after some algebraic manipulation, arrive at

$$\begin{aligned} \tilde{\psi}(k, \Delta y) &= \int_0^{L_1(\Delta y)} \tilde{\mu}_t(k, \ell) d\ell \\ &+ \frac{\exp[ikL_1(\Delta y) \operatorname{tg} \beta_2]}{\cos \beta_2} \int_{L_1(\Delta y)}^L \tilde{\mu}_t(k, \ell) \exp(-ik\ell \operatorname{tg} \beta_2) d\ell . \end{aligned} \quad (26)$$

To simplify notations, we introduce new variables, $q = k \operatorname{tg} \beta_2$, $c = \cos \beta_2$ and define two new functions: $f(z) = \tilde{\mu}(q \operatorname{ctg} \beta_2, z)$ and $F(z) = \tilde{\psi}(q \operatorname{ctg} \beta_2, \Delta y(z))$, where $\Delta y(z) = (L - z) \operatorname{tg} \beta_2$ and the dependence of the functions $f(z)$ and $F(z)$ on q is implied. Then (26) takes the form

$$\int_0^z f(\ell) d\ell + \frac{1}{c} \exp(iqz) \int_z^L \exp(-iq\ell) f(\ell) d\ell = F(z) , \quad 0 \leq z \leq L . \quad (27)$$

Solution to the above integral equation with arbitrary q and $0 < c < 1$ is obtained in Appendix B. Here we adduce the final result, which is

$$f_i(z) = -\kappa \left[G(z) - i\kappa q \exp(-i\kappa q z) \int_0^z \exp(i\kappa q \ell) G(\ell) d\ell \right] , \quad (28)$$

where

$$\kappa = \frac{c}{1-c} = \frac{\cos \beta_2}{1 - \cos \beta_2}, \quad (29)$$

$$G(z) = F'(z) - iqF(z), \quad (30)$$

prime denotes differentiation and the lower index “ i ” in $f_i(\ell)$ is used to emphasize that this is an inverse solution to Eq. (27).

One important comment on the obtained solution is necessary. The function $F(z)$ in (27) is not arbitrary but such that

$$F(L) = \exp(-i\kappa qL) \left[cF(0) + i\kappa q \int_0^L \exp(i\kappa q\ell) F(\ell) d\ell \right]. \quad (31)$$

This can be verified directly. However, experimental measurements may result in a function $F(z)$ that does not satisfy this condition. On the other hand, the inverse solution (28) is invariant if we add to $F(z)$ a function $a \exp(iqz)$ with an arbitrary constant a . It can be shown that any experimental function $F(z)$ can be uniquely written in the form $F(z) = F_{\text{reg}}(z) + a \exp(iqz)$, where $F_{\text{reg}}(z)$ satisfies condition (31). Thus, inverse formula (28) involves regularization, or filtering of input data. Full singular value analysis of the integral operators of Eqs. (27) and (28) is outside of the scope of this paper. We however, note the following. Substitution of any “probe” function $f_p(z)$ into (27), obtaining corresponding function $F(z)$, substitution of the latter into (28) will necessarily result in $f_i(z) = f_p(z)$. However, if we choose an arbitrary function $F_p(z)$, substitute it into (28) and then substitute the obtained $f_i(z)$ into (27), the resultant $F(z)$ will be, generally, not equal to $F_p(z)$.

Restoring original notations, we find the inverse solution to (26) to be

$$\begin{aligned} \tilde{\mu}_t(k, z) = & \text{ctg} \left(\frac{\beta_2}{2} \right) \left\{ H(k, z) - i\kappa \text{ctg} \left(\frac{\beta_2}{2} \right) \exp \left[-i\kappa \text{ctg} \left(\frac{\beta_2}{2} \right) z \right] \right. \\ & \left. \times \int_0^z \exp \left[i\kappa \text{ctg} \left(\frac{\beta_2}{2} \right) k\ell \right] H(k, \ell) d\ell \right\}, \end{aligned} \quad (32)$$

where

$$H(k, z) = \left[\frac{\partial}{\partial \Delta y} + ik \right] \tilde{\psi}(k, \Delta y) \Big|_{\Delta y = (L-z)\text{tg}\beta_2}. \quad (33)$$

The real space solution is then obtained by substitution of (32) into (23).

5. Numerical Simulations

Application of the analytical image reconstruction formula (32) is expected to result in faster and more accurate image reconstruction, especially when large data sets are used. However, numerical implementation of this formula is not straightforward and, in particular, requires numerical evaluation of derivative in (33). Here we illustrate image

reconstruction in SSOT using a simple numerical technique based on discretization and algebraic inversion of the two-dimensional integral equation (16).

Simulations were performed in a rectangular isotropically scattering sample with dimensions $L_x \times L_y \times L_z$. The discretization step was h and the dimensions of the sample were $L_x = 11h$, $L_y = 122h$ and $L_z = 40h$. For the case of isotropic scattering, the integral kernel in the right-hand side of Eq. (1) (known as the phase function in the transport theory) is constant: $A(\hat{\mathbf{s}}, \hat{\mathbf{s}}) = 1/4\pi$. The background absorption coefficient of the sample was equal to $0.01h^{-1}$ which was spatially modulated by absorbing inhomogeneities (the target) as is explained below. The scattering coefficient was constant throughout the sample, with three different values used: $\mu_s = 0.04h^{-1}$, $\mu_s = 0.08h^{-1}$ and $\mu_s = 0.16h^{-1}$. The sources were normally incident on the surface $z = 0$. The detectors were placed on the other side of the sample and measured the specific intensity exiting the surface $z = L_z$ at the angle of $\pi/4$ with respect to the z -axis. This included two possibilities: the exiting rays making the angle of $\pi/4$ or $3\pi/4$ with the y -axis. In some cases, data from both exit directions were used. Note that the distance L_z corresponds to the slab thickness L used in sections 3 and 4. The optical depth of the sample, $\mu_s L_z$ varied from 1.6 to 6.4. This corresponds to the mesoscopic scattering regime in which the image reconstruction method of SSOT is applicable.

5.1. Forward Problem

The forward data were obtained by solving the RTE numerically. For this purpose, we have utilized the following technique which is applicable to isotropic scattering and based on equations of Refs. [6, 7]. If $A(\hat{\mathbf{s}}, \hat{\mathbf{s}}) = 1/4\pi$, it can be shown from (3) that the specific intensity everywhere inside the sample is related to the density of electromagnetic energy $u(\mathbf{r}) \equiv \int I(\mathbf{r}, \hat{\mathbf{s}}) d^2 \hat{\mathbf{s}}$ by the following formula:

$$I(\mathbf{r}, \hat{\mathbf{s}}) = I_b(\mathbf{r}, \hat{\mathbf{s}}) + \int G_b(\mathbf{r}, \hat{\mathbf{s}}; \mathbf{r}', \hat{\mathbf{s}}') \frac{\mu_s(\mathbf{r}')}{4\pi} u(\mathbf{r}') d^3 r' d^2 \hat{\mathbf{s}}' \quad (34)$$

and that $u(\mathbf{r})$ satisfies the following integral equation

$$u(\mathbf{r}) = u_b(\mathbf{r}) + \int g_b(\mathbf{r}, \mathbf{r}') \frac{\mu_s(\mathbf{r}')}{4\pi} u(\mathbf{r}') d^3 r' , \quad (35)$$

where $g_b(\mathbf{r}, \mathbf{r}')$ is given by (7) and $u_b(\mathbf{r}) \equiv \int I_b(\mathbf{r}, \hat{\mathbf{s}}) d^2 \hat{\mathbf{s}}$ is the ‘‘ballistic density’’.

Eq. (35) is discretized on a rectangular grid and solved by methods of linear algebra. In our simulations, the sample was discretized with the step h and it was assumed that $u(\mathbf{r})$ is constant within each cubic cell. Corresponding values of $u_n = u(\mathbf{r}_n)$, where \mathbf{r}_n is the center of the n -th cubic cell, obey the algebraic system of equations with the square matrix of the size $N = L_x L_y L_z / h^3$, in our case, $N = 53,680$. The off-diagonal elements of the matrix corresponding to the integral in the right-hand side of (35) are given by $(\mu_s h^3 / 4\pi) g_b(\mathbf{r}_m, \mathbf{r}_n)$. Here we took advantage of the fact that μ_s was set to be constant throughout the sample while the inhomogeneities were purely absorbing. Computation

of the diagonal elements is slightly more involved because $g_b(\mathbf{r}, \mathbf{r}')$ diverges when $\mathbf{r} \rightarrow \mathbf{r}'$. To evaluate the diagonal elements, we need to find an approximation for the integral

$$S = \frac{\mu_s}{4\pi} \int_{V_n} g_b(\mathbf{r}_n, \mathbf{r}) d^3r, \quad (36)$$

where integration is carried out over the n -th cell. While integration over a cubic volume is difficult, the important point is that the singularity in $g_b(\mathbf{r}, \mathbf{r}')$ is integrable. We then write, approximately,

$$S \approx \mu_s \int_0^{R_{\text{eq}}} g_b(0, \mathbf{r}) r^2 dr, \quad (37)$$

where R_{eq} is the radius of a sphere of equivalent volume, i.e., $R_{\text{eq}} = (3/4\pi)^{1/3}h$. We then use $\mu_t R_{\text{eq}} \ll 1$ which allows us to write $g_b(0, \mathbf{r}) \approx 1/r^2$. This leads to $S = \mu_s R_{\text{eq}}$, and the discretized version of Eq. (35) becomes

$$(1 - \mu_s R_{\text{eq}})u_n - \frac{\mu_s h^3}{4\pi} \sum_{m \neq n} g_b(\mathbf{r}_n, \mathbf{r}_m) u_m = u_b(\mathbf{r}_n). \quad (38)$$

This set of equations is an accurate approximation to the integral equation (35) if $\mu_s R_{\text{eq}} \sim \mu_s h \ll 1$. In our simulations, $\mu_s h$ was no more than 0.16. We, however, did not neglect the term $\mu_s R_{\text{eq}}$ in the left-hand side of (38).

Eq. (38) can be written in the matrix notations as

$$\mathcal{W}|u\rangle = |b\rangle \quad (39)$$

where

$$\langle n|\mathcal{W}|m\rangle = \frac{1}{\alpha} - \frac{h^2}{|\mathbf{r}_n - \mathbf{r}_m|^2} \exp \left[- \int_0^{|\mathbf{r}_n - \mathbf{r}_m|} \mu_t (\mathbf{r}_m + \hat{\mathbf{u}}(\mathbf{r}_n - \mathbf{r}_m)\ell) d\ell \right], \quad (40)$$

α is a dimensionless coupling constant defined by

$$\alpha = \frac{\mu_s h}{4\pi(1 - \mu_s R_{\text{eq}})}, \quad (41)$$

and $\langle n|u\rangle = u_n$, $\langle n|b\rangle = 4\pi u_b(\mathbf{r}_n)/\mu_s h$. Note that the quantity $u_b(\mathbf{r}_n)$ is defined as an average over the n -th cell, namely, $u_b(\mathbf{r}_n) = h^{-3} \int_{V_n} u_b(\mathbf{r}) d^3r$.

The most time-consuming part of the forward simulation was computing the elements of matrix \mathcal{W} . The complexity arises due to the presence of inhomogeneities in the sample. Obviously, if the sample is homogeneous, integration in (40) can be performed analytically. We, however, have solved the forward problem with absorptive inclusions placed inside the sample as described in section 5.2. This required numerical computation of integrals in the right-hand side of (40). We have discretized each ray connecting the points \mathbf{r}_n and \mathbf{r}_m with the linear step $\Delta\ell = 0.1h$ and computed the

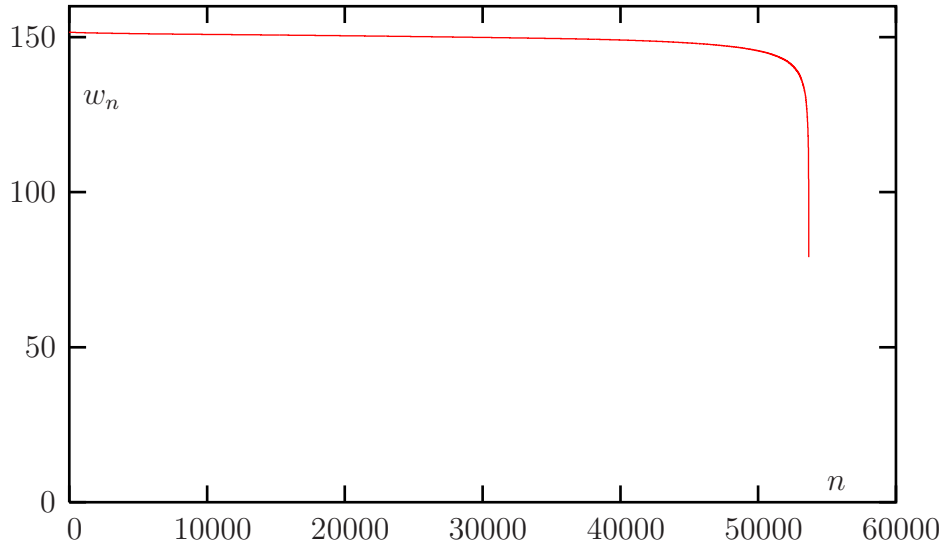


Figure 4. All 53,680 eigenvalues w_n of the matrix \mathcal{W} of Eq. 39 computed for $\mu_s = 0.08h^{-1}$ and the set of absorptive inhomogeneities described in section 5.2.

respective integrals by the trapezoidal rule. Finding all matrix elements of \mathcal{W} required computation of $N(N - 1)/2 \approx 1.4 \times 10^9$ such integrals.

After the matrix \mathcal{W} was computed, Eq. (39) was solved by direct matrix inversion. We note that the square symmetric matrix \mathcal{W} is well-posed. This is illustrated in Fig. 4 where we plot all the eigenvalues of \mathcal{W} for $\mu_s = 0.08h^{-1}$ and the set of absorptive inhomogeneities described in section 5.2. It can be seen that the condition number of \mathcal{W} does not exceed, approximately, 2. We also note that \mathcal{W} is positive-definite which is the reflection of the fact that both u and u_b are positive. We have also verified that, in all simulations, the “diffuse” component of the density u_d defined by $u_d = u - u_b$ was positive everywhere inside the sample.

The data function of SSOT requires the knowledge of the specific intensity $I(\mathbf{r}, \hat{\mathbf{s}})$ rather than the density $u(\mathbf{r})$. We have computed the specific intensity by substituting the numerical solution $u(\mathbf{r}_n)$ into (34) (where the ballistic part I_b may be ignored). The corresponding integration was performed numerically. Note that $I(\mathbf{r}, \hat{\mathbf{s}})$ obtained from (34) satisfies the boundary conditions at all surfaces. We also stress that the numerical approach described in this section is non-perturbative and includes all orders of the scattering-order expansion.

An important consideration is the effects of discretization on the expression for single-scattering intensity (10) that is used in the definition of data function according to (13), and on the expression for the forward data according (34). Since discretized computations involve discrete rays, the delta-function $\delta(|\varphi_{\hat{\mathbf{s}}_1} - \varphi_{\hat{\mathbf{s}}_2}| - \pi)$ and the geometrical factor $1/r_{21} \sin \theta_2 \sin \theta_1$ must be modified. In particular, the expression for the single-scattered intensity (the discrete analog of (10)) is

$$I_s(\mathbf{r}_2, \hat{\mathbf{s}}_2; \mathbf{r}_1, \hat{\mathbf{s}}_1) = \frac{\mu_s h^3}{4\pi} g_b(\mathbf{r}_2, \mathbf{R}_{21}) u_b(\mathbf{R}_{21}) . \quad (42)$$

where $u_b(\mathbf{R}_{21})$ is the average of $u_b(\mathbf{r})$ over the volume of the cell that contains \mathbf{R}_{21} . The definition of the data function must be modified accordingly. The discretized version of (34) is

$$I(\mathbf{r}_2, \hat{\mathbf{s}}_2) = \frac{\mu_s h^3}{4\pi} \sum_{\hat{\mathbf{u}}(\mathbf{r}_2 - \mathbf{r}_n) = -\hat{\mathbf{s}}_2} g_b(\mathbf{r}_2, \mathbf{r}_n) u_n, \quad (43)$$

where u_n must be computed numerically for the selected source. The condition $\hat{\mathbf{u}}(\mathbf{r}_2 - \mathbf{r}_n) = -\hat{\mathbf{s}}_2$ means that summation is performed only over such cells that are intersected by the ray exiting from the detection point \mathbf{r}_2 in the direction $-\hat{\mathbf{s}}_2$. The above formula is valid for the specific measurement scheme we have used in numerical simulations when the intersection length of all such rays with any cubic cell is constant. If this is not so, a more complicated numerical integration must be employed. Finally, we emphasize that the account of geometrical factors in (10) is important if experimental data are used. At the same time, the use of experimental data avoids many mathematical complications that arise due to discretization of rays.

To model noise in the measured data, we first scaled and rounded off the specific intensity obtained from the forward solver so that it was represented by 16-bit integers, similar to measurement by digital ccd cameras. Then a statistically-independent positively-defined random variable was added to each measurement. The random variables were evenly distributed in the interval $[0, nI_{\text{av}}]$, where n is the noise level indicated in the figure legends below and I_{av} is the average measured intensity (a 16-bit integer). We did not subtract the ‘‘dc part’’ (the positive background) of the intensity. Then the simulated intensity measurements, together with the appropriately scaled incident intensity I_0 were substituted into (13) to obtain the data function ϕ .

5.2. Inverse Problem

The target was a set of absorbing inclusions formed in the shape of letters, with absorption varying from $0.06h^{-1}$ to $0.2h^{-1}$. The inclusions were concentrated only in three layers: $x = 3h$, $x = 6h$ and $x = 9h$, as shown in the columns marked ‘‘model’’ of Figs. 6-8. Thus, for example, in the case $\mu_s = 0.04h^{-1}$ the contrast of μ_t (the ratio of μ_t in the target to the background value) varied from 2.0 in the letters ‘‘RADIOL’’ to 4.8 in the letters ‘‘DEPT’’. In the case $\mu_s = 0.16h^{-1}$, the contrast was smaller and varied from 1.18 to 2.12.

Eq. (16) was discretized on the same grid as was used for obtaining the forward solution in section 5.1, except that planar slices with fixed x -coordinates were used in the image reconstruction. The discrete version of (16) has the form

$$\sum_n \mathcal{L}_{\nu n} \mu_{tn} = \phi_\nu, \quad (44)$$

where $\mathcal{L}_{\nu n}$ is the length of the intersection of the SSR indexed by $\nu = (y_1, y_2)$ (y_1 and y_2 are the discrete y -coordinates of the source and detector) with the n -th cubic cell (located within the selected x -slice of the sample). In our simulations, only three possibilities

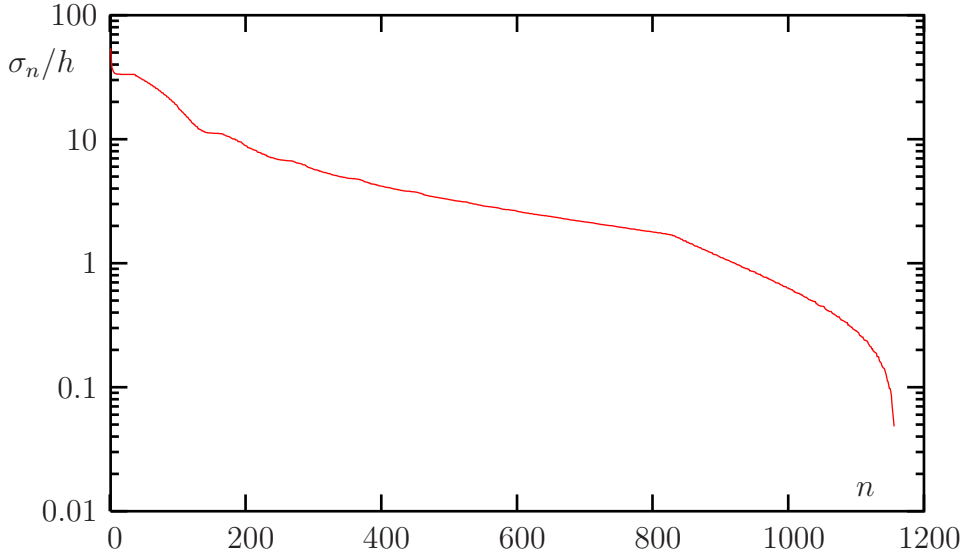


Figure 5. All 1,156 non-zero singular values σ_n of the matrix \mathcal{L} (the size of \mathcal{L} in this example is $1,600 \times 1,156$).

existed: $\mathcal{L}_{\nu n} = h$, $\mathcal{L}_{\nu n} = \sqrt{2}h$, or $\mathcal{L}_{\nu n} = 0$. The vast majority of the elements of \mathcal{L} were zero (for such combination of the indices ν and n that the corresponding ray did not intersect the n -th cell). The actual values of elements of \mathcal{L} were determined from trivial geometric considerations which are not repeated here. The matrix form of (44) is

$$\mathcal{L}|\mu_t\rangle = |\phi\rangle \quad (45)$$

with the obvious meaning of notations $|\mu_t\rangle$ and $|\phi\rangle$. The equation (45) was solved by regularized SVD pseudoinverse [8], namely,

$$|\mu_t^+\rangle = (\mathcal{L}^*\mathcal{L})^{-1}\mathcal{L}^*|\phi\rangle. \quad (46)$$

Here $(\mathcal{L}^*\mathcal{L})^{-1}$ is understood in the following sense:

$$(\mathcal{L}^*\mathcal{L})^{-1} = \sum_n \Theta(\sigma_n^2 - \epsilon) \frac{|g_n\rangle\langle g_n|}{\sigma_n^2}, \quad (47)$$

where $\Theta(x)$ is the step function, ϵ is a small regularization parameter and $|g_n\rangle$, σ_n are the singular functions and singular values, respectively, of the matrix \mathcal{L} . Numerically, these are found by solving the symmetric eigenproblem $\mathcal{L}^*\mathcal{L}|g_n\rangle = \sigma_n^2|g_n\rangle$. A typical spectrum of singular values of \mathcal{L} for $\mu_s = 0.08h^{-1}$, 1,600 measurements and $34^2 = 1,156$ unknown values of μ_t (the size of \mathcal{L} in this example is $1,600 \times 1,156$, so that the problem is slightly overdetermined) is shown in Fig. 5. It can be seen that the condition number for the inverse problem is much larger than for the forward problem. In the example shown in Fig. 5, the condition number is $\approx 10^3$. Thus, the inverse problem is very mildly ill-posed.

Reconstruction of the total attenuation coefficient μ_t was performed in slices $x = x_{\text{slice}} = \text{const}$ separated by the distance $\Delta x = h$. For each slice, the source

positions were $x = x_{\text{slice}}$, $y = nh$, $z = 0$, with n being integers. Seven consecutive slices were obtained, starting from the slice $x_{\text{slice}} = 3h$. The reconstruction area inside each slice was $44h \leq y \leq 77h$, $4h \leq z \leq 37h$, with the field of view $34h \times 34h$.

The results of image reconstruction are shown in Figs. 6-8 where we show all seven slices separated by $\Delta x = h$. At the noise levels $n = 0$ and $n = 1\%$, only the rays making the angle $\pi/4$ with the y -axis were used; for the noise level $n = 3\%$, the exiting rays which make the angle $3\pi/4$ with the y -axis were also used to improve image stability.

It can be seen that the spatial resolution of images depends on the noise level and contrast and can be as good as one discretization step, h . reconstruction is stable in the presence of noise and quantitative (note that all panels in each figure are plotted using the same color scale). When $\mu_s = 0.16h^{-1}$ (Fig.) the optical depth of the sample is $\mu_s L_z = 6.4$. This is a borderline case when scattering is sufficiently strong so that the single-scattering approximation of SSOT may be expected to be inaccurate. Indeed, the image quality in Fig. 8 is markedly worse than in Figs. 6,7, yet, the letters in the image remain legible. Overall, reconstructions demonstrate the image quality and level of detail which is customary in x-ray tomography but can be hardly expected in optical tomography with multiply scattered light.

It should be also noted that the absolute values of the reconstructed regularization coefficients are not sensitive to the value of regularization's parameter ϵ in the regularized pseudoinverse solution (formula (47)). Qualitatively same results are obtained by setting $\epsilon = 0$, although we found that selecting a small but nonzero value of ϵ tends to slightly improve the visual appearance of images.

- [1] J. C. Schotland and V. A. Markel, "Inverse scattering with diffusing waves," *J. Opt. Soc. Am. A*, vol. 18, no. 11, pp. 2767–2777, 2001.
- [2] V. A. Markel and J. C. Schotland, "Inverse scattering for the diffusion equation with general boundary conditions," *Phys. Rev. E*, vol. 64, no. 3, p. R035601, 2001.
- [3] V. A. Markel and J. C. Schotland, "Effects of sampling and limited data in optical tomography," *Appl. Phys. Lett.*, vol. 81, no. 7, pp. 1180–1182, 2002.
- [4] V. A. Markel, V. Mital, and J. C. Schotland, "The inverse problem in optical diffusion tomography. iii. inversion formulas and singular value decomposition," *J. Opt. Soc. Am. A*, vol. 20, no. 5, pp. 890–902, 2003.
- [5] V. A. Markel and J. C. Schotland, "Symmetries, inversion formulas and image reconstruction for optical tomography," *Phys. Rev. E*, vol. 70, no. 5, p. 056616(19), 2004.
- [6] R. C. Erdmann and C. E. Siewert, "Green's function for the one-speed transport equation in spherical geometry," *J. Math. Phys.*, vol. 9, no. 1, pp. 81–89, 1968.
- [7] E. W. Larsen, "Solutions of the steady, one-speed neutron transport equation for small mean free paths," *J. Math. Phys.*, vol. 15, no. 3, pp. 299–305, 1974.
- [8] F. Natterer and F. Wubbeling, *Mathematical methods in image reconstruction*. Philadelphia: SIAM, 2001.

Appendix A. Derivation of Formula (10)

Substitution of (5) into (9) with $\mathbf{r} = \mathbf{r}_2$ and $\hat{\mathbf{s}} = \hat{\mathbf{s}}_2$ results in the following expression for the single-scattered intensity:

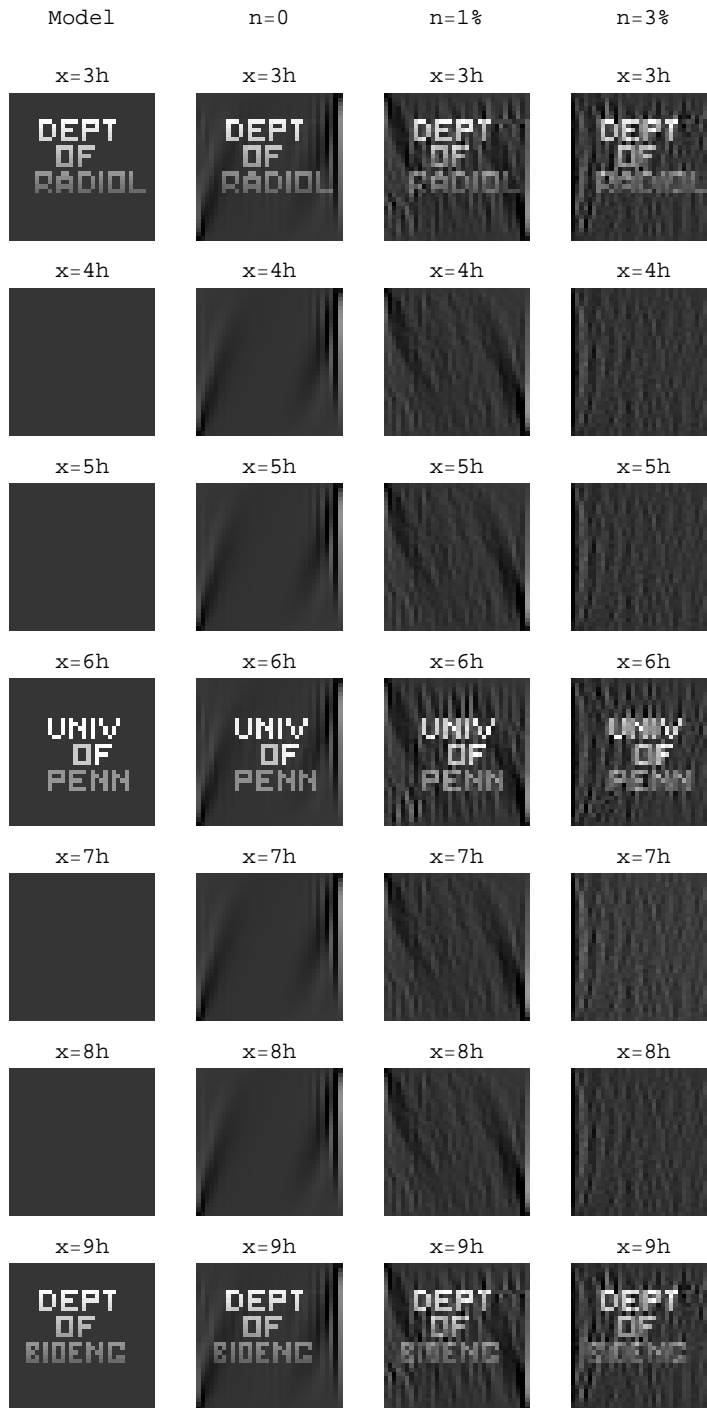


Figure 6. Image reconstruction for $\mu_s = 0.04h^{-1}$. The same color scale is used for all panels with the maximum (white) corresponding to $\mu_t = 0.24h^{-1}$ and the minimum (black) to $\mu_t = 0$.

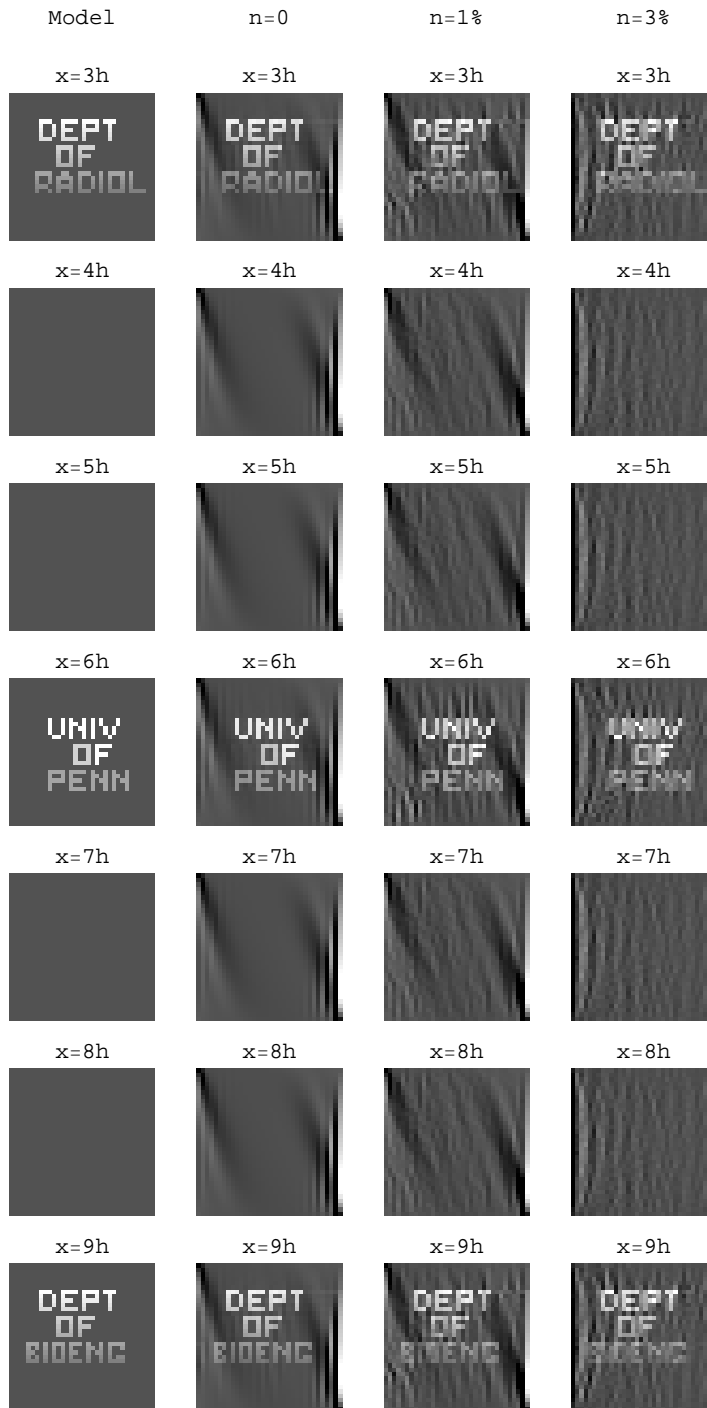


Figure 7. Image reconstruction for $\mu_s = 0.08h^{-1}$. The same color scale is used for all panels with the maximum (white) corresponding to $\mu_t = 0.28h^{-1}$ and the minimum (black) to $\mu_t = 0$.

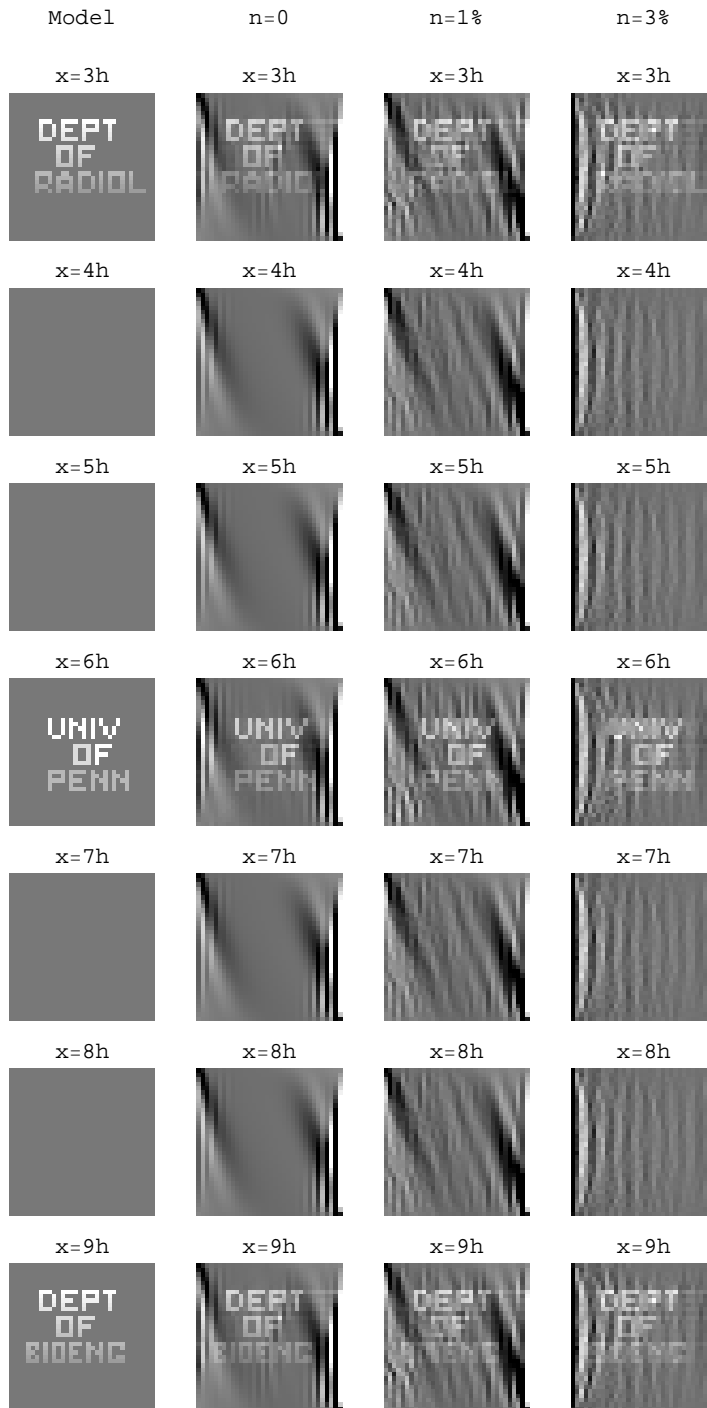


Figure 8. Image reconstruction for $\mu_s = 0.16h^{-1}$. The same color scale is used for all panels with the maximum (white) corresponding to $\mu_t = 0.36h^{-1}$ and the minimum (black) to $\mu_t = 0$.

$$I_s(\mathbf{r}_2, \hat{\mathbf{s}}_2; \mathbf{r}_1, \hat{\mathbf{s}}_1) = I_0 A(\hat{\mathbf{s}}_2, \hat{\mathbf{s}}_1) \int \mu_s(\mathbf{r}) g_b(\mathbf{r}_2, \mathbf{r}) g_b(\mathbf{r}, \mathbf{r}_1) \times \delta_2[\hat{\mathbf{u}}(\mathbf{r}_2 - \mathbf{r}) - \hat{\mathbf{s}}_2] \delta_2[\hat{\mathbf{u}}(\mathbf{r} - \mathbf{r}_1) - \hat{\mathbf{s}}_1] d^3 r . \quad (\text{A.1})$$

With the change of variables $\mathbf{r} = \mathbf{r}_1 + \mathbf{R}$, $\mathbf{R} = R\hat{\mathbf{R}}$ and $d^3 r = d^3 R = R^2 dR d^2 \hat{R}$, the integral over $d^2 \hat{R}$ is immediately evaluated and we transform (A.1) into the following one-dimensional integral

$$I_s(\mathbf{r}_2, \hat{\mathbf{s}}_2; \mathbf{r}_1, \hat{\mathbf{s}}_1) = I_0 A(\hat{\mathbf{s}}_2, \hat{\mathbf{s}}_1) \int g_b(\mathbf{r}_2, \mathbf{r}_1 + R\hat{\mathbf{s}}_1) g_b(\mathbf{r}_1 + R\hat{\mathbf{s}}_1, \mathbf{r}_1) \times \mu_s(\mathbf{r}_1 + R\hat{\mathbf{s}}_1) \delta_2[\hat{\mathbf{u}}(\mathbf{r}_{21} - R\hat{\mathbf{s}}_1) - \hat{\mathbf{s}}_2] R^2 dR . \quad (\text{A.2})$$

We then write the remaining delta-function as

$$\delta_2(\hat{\mathbf{u}} - \hat{\mathbf{s}}_2) = \delta(\varphi_{\hat{\mathbf{u}}} - \varphi_{\hat{\mathbf{s}}_2}) \delta(\cos \theta_{\hat{\mathbf{u}}} - \cos \theta_{\hat{\mathbf{s}}_2}) . \quad (\text{A.3})$$

Here $\mathbf{u} = \mathbf{r}_{21} - R\hat{\mathbf{s}}_1$ and θ and φ are polar angles of the respective unit vectors. We choose a reference frame so that its z -axis coincides with the source-detector line. We then find that $\varphi_{\hat{\mathbf{u}}} = \varphi_{\hat{\mathbf{s}}_1} \pm \pi$. Consequently,

$$\delta(\varphi_{\hat{\mathbf{u}}} - \varphi_{\hat{\mathbf{s}}_2}) = \delta(|\varphi_{\hat{\mathbf{s}}_1} - \varphi_{\hat{\mathbf{s}}_2}| - \pi) . \quad (\text{A.4})$$

We next write

$$\delta(\cos \theta_{\hat{\mathbf{u}}} - \cos \theta_{\hat{\mathbf{s}}_2}) = \delta[f(R)] , \quad (\text{A.5})$$

where

$$f(R) = \frac{r_{21} - R \cos \theta_1}{\sqrt{r_{21}^2 - 2r_{21}R \cos \theta_1 + R^2}} - \cos \theta_2 . \quad (\text{A.6})$$

It is not difficult to see that if $\theta_1 + \theta_2 \geq \pi$, equation $f(R) = 0$ has no positive roots. In the opposite case, however, there is one positive root $R = L_1$. Lengths L_1 and L_2 are given by formula (12) and illustrated in Fig. 2. We thus have

$$R^2 \delta[f(R)] = \Theta(\pi - \theta_1 - \theta_2) L_1^2 \frac{\delta(R - L_1)}{|f'(L_1)|} , \quad (\text{A.7})$$

where prime denotes derivative. Computation of the derivative is straightforward and yields

$$|f'(L_1)| = \frac{L_1}{r_{21} L_2 \sin^2(\theta_1 + \theta_2)} . \quad (\text{A.8})$$

Collecting all the expressions, we arrive at

$$R^2 \delta_2[\hat{\mathbf{u}}(\mathbf{r}_{21} - R\hat{\mathbf{s}}_1) - \hat{\mathbf{s}}_2] = \delta(|\varphi_{\hat{\mathbf{s}}_1} - \varphi_{\hat{\mathbf{s}}_2}| - \pi) \Theta(\pi - \theta_1 - \theta_2) \frac{r_{21} L_1 L_2 \delta(R - L_1)}{\sin^2(\theta_1 + \theta_2)} . \quad (\text{A.9})$$

We then recall that $\mathbf{r}_1 + L_1 \hat{\mathbf{s}} = \mathbf{R}_{21}$, $L_1 = |\mathbf{R}_{21} - \mathbf{r}_1|$, $L_2 = |\mathbf{r}_2 - \mathbf{R}_{21}|$ and obtain

$$g_b(\mathbf{r}_2, \mathbf{r}_1 + L_1 \hat{\mathbf{s}}_1) = \frac{1}{L_2^2} \exp \left[- \int_0^{L_2} \mu_t(\mathbf{R}_{21} + \hat{\mathbf{s}}_2 \ell) d\ell \right] , \quad (\text{A.10})$$

$$g_b(\mathbf{r}_1 + L_1 \hat{\mathbf{s}}_1, \mathbf{r}_1) = \frac{1}{L_1^2} \exp \left[- \int_0^{L_1} \mu_t(\mathbf{r}_1 + \hat{\mathbf{s}}_1 \ell) d\ell \right] . \quad (\text{A.11})$$

Finally, using expressions (12) for L_1 and L_2 and substituting everything back into (A.2), we arrive at the result (10).

Appendix B. Solution of the Integral Equation (27).

To solve

$$\int_0^z f(\ell) d\ell + \frac{1}{c} \exp(iqz) \int_z^L \exp(-iq\ell) f(\ell) d\ell = F(z) \quad (\text{B.1})$$

for $f(z)$, we differentiate (B.1) once with respect to z to obtain

$$F'(z) = -\frac{1}{\kappa} f(z) + \frac{iq}{c} \exp(iqz) \int_z^L \exp(-iq\ell) f(\ell) d\ell , \quad (\text{B.2})$$

where $\kappa = c/(1 - c)$. Now we use (B.1) and (B.2) to find the linear combination $G(z) = F'(z) - iqF(z)$. The result is

$$G(z) = -\frac{1}{\kappa} f(z) - iq \int_0^z f(\ell) d\ell . \quad (\text{B.3})$$

Differentiating once more with respect to z , we obtain the following differential equation

$$f'(z) + i\kappa q f(z) = -\kappa G'(z) , \quad (\text{B.4})$$

which has the obvious solution

$$y_i(z) = \exp(-i\kappa qz) \left[f(0) - \kappa \int_0^z \exp(i\kappa q\ell) G'(\ell) d\ell \right] . \quad (\text{B.5})$$

We then set $z = 0$ in (B.3) and find that $f(0) = -\kappa G(0)$. Substituting this into (B.5) and integrating once by parts, we arrive at the inverse solution (28).